Performance Bounds for a Maxima-Sampling Envelope Detector

Swagat Bhattacharyya, *Member, IEEE*

Abstract—Envelope detectors in automatic gain control systems must achieve both low tracking latency and low output ripple for feedback stability. Conventional non-sampled envelope detectors intrinsically trade off latency and ripple. Maxima-sampling envelope detectors (MSEDs), which demodulate by sampling signal peaks, circumvent this latency-ripple trade-off, enabling control loops that remain stable over several frequency decades. However, MSED nonlinearity causes an intricate, previously uncharacterized interplay between input spectral properties and performance. This work analytically derives and numerically verifies input-dependent performance bounds for MSEDs. By formulating practical "rules-of-thumb" for mixed-signal circuit designers, we pave the way for the broader adoption of MSEDs.

Index Terms—Extrema Sampling, Nonuniform Sampling, Envelope Detection, Aliasing, Piecewise Linearization

I. INTRODUCTION

AUTOMATIC gain control (AGC) circuits in oscillatory systems rely on envelope detectors for accurate state estimation. Envelope detectors for mixed-signal control systems need both low tracking latency and low output ripple to maintain a stable feedback loop [1], [2]. Non-sampled envelope detectors (NSEDs), implemented using rectifying or square-law circuits [3] or digital algorithms [4], have traditionally predominated in envelope detector applications. NSED-based designs are well-suited for steady-state tracking in applications with a stationary carrier frequency, such as RF envelope detectors and audio volume unit meters. However, NSED designs are inherently limited by a trade-off between latency and ripple (Fig. 1), which is detrimental when the carrier frequency varies over decades or when the modulation signal changes rapidly. This latency-ripple trade-off is reflected in the analytical framework used for NSEDs, which treats the envelope detector as a modest nonlinearity embedded within an otherwise linear time-invariant (LTI) system [5].

A majority of contemporary work has concentrated on proposing innovative nonlinearities to improve the latency of NSEDs. While these contemporary approaches can offer notable improvements, they are still constrained by two major limitations: they can not fully eliminate the latency-ripple trade-off, and their nonlinearities can pose severe challenges for analytical modeling and subsequent integrated circuit designs. For instance, [5] addresses the latency–ripple trade-off by employing a topology that cascades a high-ripple rectifying circuit with an adaptive ripple filter whose time constant varies dynamically with the input amplitude. The
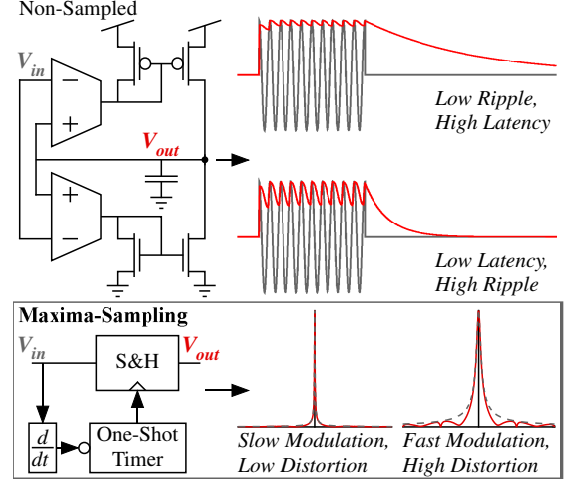
Fig. 1. Envelope detectors have intrinsic trade-offs. Conventional non-sampled envelope detectors (NSEDs) trade latency and ripple. An emerging paradigm, maxima-sampling envelope detectors (MSEDs), avoid an latency–ripple trade-off, with performance instead being determined by input aliasing. This work introduces a mathematical framework for analyzing MSED performance.

design in [5] achieves an excellent linearity of 1 dB over a 70 dB dynamic range in sinusoidal steady state. However, the expansion-based modeling approach proposed in [5] does not accurately capture behavior during rapid transients, limiting the use of models to tuning purposes. Similarly, [6] presents a radio-frequency envelope detector using an additional current source to accelerate the falling edges of the envelope, thereby improving latency. Yet, despite performing well from 1 GHz to 10 GHz, the approach in [6] is sensitive to the selection of an integration capacitance and can not maintain its performance over decades of frequency due to its constant integration rate.

Maxima-sampling envelope detectors (hereafter, MSEDs) adopt a fundamentally different approach by demodulating via peak sampling (Fig. 1). Peak sampling circumvents a latency–ripple trade-off [7], facilitating the design of AGC loops that remain stable over many decades of frequency. The application of maxima sampling to envelope detection is in its early stages. Previous related research has mainly focused on the use of extrema sampling for nonuniform analog-to-digital converters [8], [9], [10] and the mathematical treatment thereof [11], [12]. An early investigation of MSEDs [7] introduced a novel topology that achieved significant improvements in settling time, output ripple, and dynamic range compared to non-sampled designs in similar process nodes. Recently, [2] showed an amplitude- and voltage-controlled oscillator with the widest-reported tuning range for an amplitude-regulated
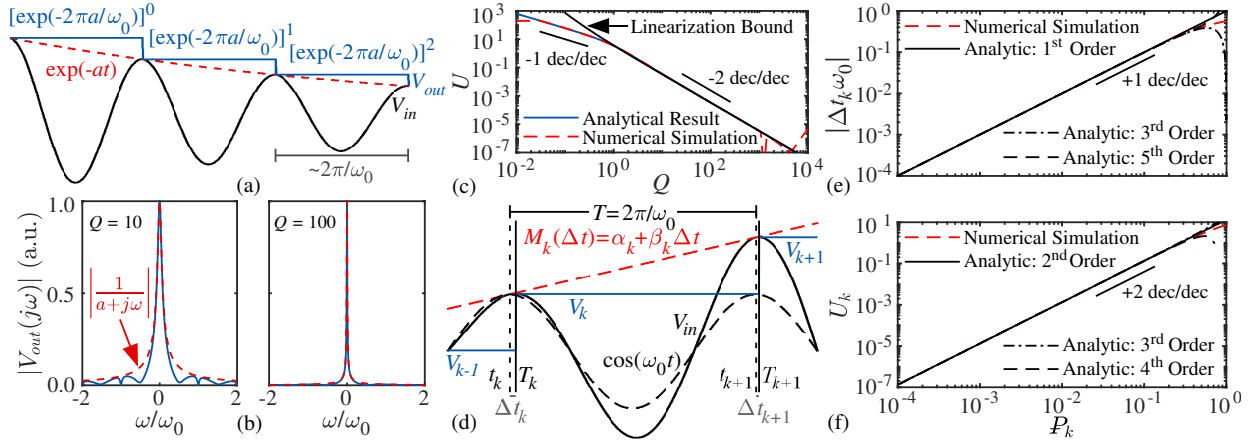
Fig. 2. (a) Annotated MSED V_{in} and V_{out} for Section II derivations. (b) Frequency-domain view of MSED aliasing during exponential modulation. (c) Comparison of normalized error signal energy from analytical expression (Eq. 2), piecewise linearization (Eq. 3), and numerical simulation. (d) Geometric basis of the time-domain analyses in Section III, where the modulation signal is approximated piecewise via line segments between carrier signal maxima. Numerical simulation compared to analytical predictions of (e) normalized maxima timestamp shift (Eq. 8) and (f) U_k (Eq. 12) from piecewise-linear modulation.

oscillator of the selected topology. This wide tuning range was enabled by an AGC using a hybrid NSED-MSED design.

Despite recent progress, the mathematical framework for analyzing MSEDs remains underdeveloped, with prior designs relying on empirical or ad-hoc methods. From a circuits perspective, MSEDs extract input maxima using a sample-and-hold (S&H) clocked by pulses on negative-going zero crossings of the input derivative (Fig. 1). MSED operation intuitively amounts to nonuniformly sampling at half the local carrier frequency, thereby leveraging aliasing to demodulate the input to baseband. MSEDs enable rapid envelope extraction (i.e., within one carrier cycle) but also introduce distortion from undesired aliasing. MSED performance thus depends on the relative strength of desired versus undesired aliasing effects, which in turn depends on input properties. Circuit designers need practical guidelines and performance guarantees given input dependencies to readily adopt MSEDs in wideband mixed-signal feedback systems such as AGC loops in voltage-controlled oscillators or burst-mode systems.

This work analytically derives and numerically verifies performance bounds for MSEDs based on both time-domain and frequency-domain signal properties. We show that MSED performance depends on the local rate of change of the modulation signal relative to the carrier frequency, and we establish practical "rules-of-thumb" to guide mixed-signal circuit designers. Our novel contributions include:

- A unified analytical framework for predicting MSED behavior in response to generic envelope signals.
- Tight performance bounds for special envelope signals.
- *Experiment-driven* motivation of physical considerations.

Analysis code and full derivations are hosted at: https://github. com/SwagatBhattacharyya/Maxima-Sampling. This work proceeds stepwise by (1) studying exponential modulation, (2) generalizing bounds via time-domain analysis, (3) reformulating bounds using spectral properties, and (4) discussing physical considerations via an experiment-driven approach.

II. FREQUENCY-DOMAIN INTUITION

Undesired aliasing, which occurs in the presence of any amplitude-modulated input, limits MSED performance. Let us first consider the unitless finite-energy test signal $V_{in}(t) = \cos(\omega_0 t)\exp(-at)\Theta(t)$, where $a > 0$, and $\Theta(t)$ denotes the unit step (Fig. 2(a)). This V_{in} arises as the natural response of an underdamped second-order system with quality factor $Q = \omega_0/2a$ and approximates the local behavior of many electronic oscillators. Aliasing can be studied by modeling a MSED as an impulse-train sampler clocked at ω_0 followed by a zero-order hold [2]. The output spectrum is then:

$$V_{out}(j\omega) = \sum_{k=-\infty}^{\infty} \left(\frac{\exp\left(-j\pi\omega/\omega_0\right)}{a + j(\omega - k\omega_0)} \cdot \frac{\sin\left(\pi\omega/\omega_0\right)}{\pi\omega/\omega_0} \right). \quad (1)$$

Figure 2(b) shows $V_{out}(j\omega)$ for both low and high Q. Note that throughout this work, all plotted quantities are dimensionless (unless specified otherwise). Figure 2(b) shows that at low Q, the spectrum is quite distorted, while at high Q, $V_{out}(j\omega)$ approaches the spectrum of the modulation signal. While useful for visualization, this frequency-domain representation is not amenable to quantifying aliasing extent, as each summand in Eq. 1 has infinite spectral support. To quantify the severity of undesired aliasing, we define U: the ratio of the demodulation error signal energy to the modulation signal energy. We compute U through a time-domain approach:

$$U = \int_0^\infty |V_{out}(t) - \exp(-at)|^2 dt \Big/ \int_0^\infty |\exp(-at)|^2 dt$$

$$\approx 2a \sum_{k=0}^\infty \exp\left(-\frac{2\pi k}{Q}\right) \int_0^{2\pi/\omega_0} \left[1 - \exp(-a\tau)\right]^2 d\tau \quad (2)$$

$$= \frac{4\exp(-\pi/Q) - \exp(-2\pi/Q) + 2\pi/Q - 3}{1 - \exp(-2\pi/Q)}.$$

Figure 2(c) plots the final approximation in Eq. 2 alongside the numerical solution of its original integral formulation as computed using 'ode89' and numerical peak finding. Figure 2(c) shows a steep trade-off between Q and undesired aliasing severity U. The two methods shown in Fig. 2(c) are in good

agreement in their respective regimes of validity. At low Q, a key assumption underlying Eq. 2 (i.e., negligible maxima perturbation) is not valid, and at high Q, numerical simulation accuracy degrades due to integration error. These analyses imply that the input envelope must vary slowly over each carrier period for an undistorted envelope estimate.

Extending the analytical methods in this section is neither easy nor necessary for most applications. Moreover, we must relax the implicit assumption of pseudo-uniform sampling, as maxima sampling is inherently nonuniform. We propose time-domain analysis based on a piecewise linearization of the modulation signal as a means to address the poor complexity scaling of prior methods. As a preview of its efficacy, the black trace in Fig. 2(c) shows the linearization-based prediction (found by substituting $P_k = 1/2Q$ into Eq. 12):

$$U \sim 1/3Q^2 + \pi/8Q^3. \tag{3}$$

Eq. 3 is tight for high Q, where modulation is slow relative to the carrier rate; Eq. 3 is not tight at low Q due to the invalid assumption of negligible higher-order terms in $M(t)$.

III. PIECEWISE TIME-DOMAIN ANALYSIS

Consider a real-valued amplitude-modulated MSED input of form: $V_{in}(t) = M(t)\cos(\omega_0 t)$, where $M(t) > 0$ ($\forall t \in \mathbb{R}$), which ensures nonzero input signal energy over any carrier period and no inversion in the relative carrier phase. The geometry underlying our piecewise analysis is shown in Fig. 2(d), and our approach is as follows: (1) find the modulation-induced maxima timestamp shift (Δt_k), (2) find integration bounds and maxima values (V_k) from Δt_k, (3) estimate the local undesired aliasing severity U_k based on V_k and Δt_k, and (4) show how to estimate U_k for a test signal.

A. Estimation of Maxima Timestamps

We start our estimation of input maxima timestamps by enforcing the first derivative constraint on $V_{in}(t)$:

$$\dot{M}(t)/M(t) = \omega_0 \tan(\omega_0 t). \tag{4}$$

We assume $M(t)$ can be linearized everywhere; a sufficient condition for linearizability is that $M(t)$ be bandlimited to some bandwidth Ω—in which case the Paley-Wiener Theorem [13] assures that $M(t)$ is in C^∞. We denote the linearization of $M(t)$ about the kth carrier signal maximum as: $M_k(\Delta t) := \alpha_k + \beta_k \Delta t$. The maxima of the carrier signal $\cos(\omega_0 t)$ occur at $t_k = Tk = 2\pi k/\omega_0$ ($\forall k \in \mathbb{Z}$), and the modulation-induced shift in maxima timestamps (denoted $\Delta t_k := T_k - t_k$) can be estimated by invoking a small-angle approximation on Eq. 4:

$$\frac{\beta_k/\omega_0^2}{\alpha_k + \beta_k \Delta t_k} \approx \Delta t_k \rightarrow \Delta t_k \approx -\frac{\alpha_k}{2\beta_k} + \frac{\sqrt{\omega_0^2 \alpha_k^2 + 4\beta_k^2}}{2\omega_0 \beta_k}. \tag{5}$$

To manage "entropy" in further derivations, we invoke the intuition from Section II, which found only the *relative* rate of change between the modulating and carrier signal relevant. We thus normalize timescales to the carrier period by defining:

$$P_k := \frac{M_k(T) - M_k(0)}{M_k(0)} = \frac{\beta_k T}{\alpha_k} = \frac{2\pi\beta_k}{\alpha_k\omega_0}, \quad \mathcal{P}_k := \frac{P_k}{2\pi}, \tag{6}$$
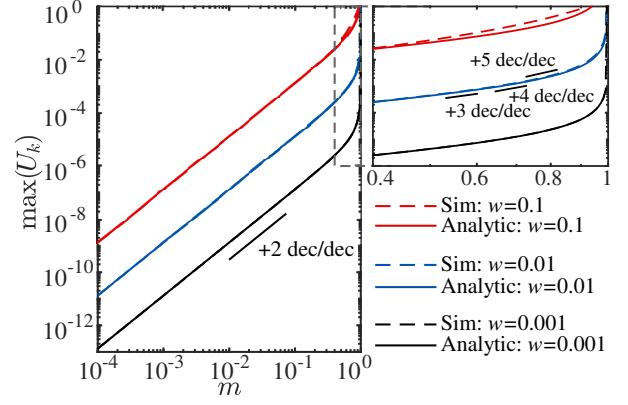

Fig. 3. Worst-case bounds on undesired aliasing severity metric U under sinusoidal modulation computed as analytically (Eq. 16) and numerically.

where P_k denotes the 'Percent' increase in $M(t)$ between carrier maxima. Expanding the root in Eq. 5 about $\beta_k = 0$:

$$\sqrt{\omega_0^2 \alpha_k^2 + 4\beta_k^2} = \sum_{n=0}^{\infty} \left[\left(4\beta_k^2\right)^n \left(\omega_0^2 \alpha_k^2\right)^{\frac{1}{2}-n} \binom{1/2}{n} \right]$$
$$= \alpha_k \omega_0 \sum_{n=0}^{\infty} \left[\zeta_n P_k^{2n} \right]; \quad \zeta_n = \frac{(-1)^{n+1}(2n)!}{(2n-1)(n!)^2}, \tag{7}$$

where the region of convergence is $|P_k| < 1/2$. We now isolate Δt_k by substituting Eq. 7 into Eq. 5 and simplifying:

$$\Delta t_k \approx \sum_{n=1}^{\infty} \left[\frac{\zeta_n P_k^{2n-1}}{2\omega_0} \right]; \zeta_n = \begin{cases} \dfrac{6-4n}{n}\zeta_{n-1}, & n > 1 \\ 2, & n = 1 \end{cases}. \tag{8}$$

Figure 2(e) compares partial sums of Eq. 8 to numerical simulation. Agreement between theory and numerical simulation is excellent when $P_k < 1/2\pi$, which makes the small-angle approximation used for Eq. 5 valid. When $P_k < 1/2\pi$, the first-order term suffices for most computations since its magnitude tightly bounds the value of $|\Delta t_k|$ (due to the alternating signs and rapidly decaying magnitude of subsequent terms). To first order, the timestamp of the kth peak of $V_{in}(t)$ is:

$$T_k = t_k + \Delta t_k \approx \left(2\pi k + P_k\right)/\omega_0; \quad (P_k < 1/2\pi). \tag{9}$$

B. Piecewise Analytic Estimation of Undesired Aliasing

We estimate the undesired aliasing severity between the kth and (k+1)th peak (U_k) by normalizing the demodulation error:

$$U_k := \frac{\dfrac{1}{T}\displaystyle\int_{\Delta t_k}^{T+\Delta t_{k+1}} \left[V_k - M_k(t)\right]^2 dt}{\dfrac{1}{T}\displaystyle\int_{\Delta t_k}^{T+\Delta t_{k+1}} M_k(t)^2 dt}, \tag{10}$$

where MSED hold level (V_k) follows by inserting Δt_k (Eq. 8) into a parabolic approximation of V_{in}: $V_k = \alpha_k + \beta_k \Delta t_k - \alpha_k \omega_0^2 \Delta t_k^2/2 + \mathcal{O}\left(\Delta t_k^3\right)$. Substituting V_k into Eq. 10 yields:

$$U_k \approx \frac{\displaystyle\int_0^{T(1-\mathcal{P}_k^2)} \left[\beta_k \tau + \alpha_k \omega_0^2 \Delta t_k^2/2 + \mathcal{O}\left(\Delta t_k^3\right)\right]^2 d\tau}{T\alpha_k^2 \left(1 + 2\pi\mathcal{P}_k + \mathcal{O}\left(\mathcal{P}_k^2\right)\right)} \tag{11}$$
$$= \frac{4\pi^2\beta_k^2/3\omega_0^2 + \pi\beta_k\alpha_k\omega_0\Delta t_k^2 + \mathcal{O}\left(\Delta t_k^3\right)}{\alpha_k^2\left(1 + 2\pi\mathcal{P}_k + \mathcal{O}\left(\mathcal{P}_k^2\right)\right)}.$$
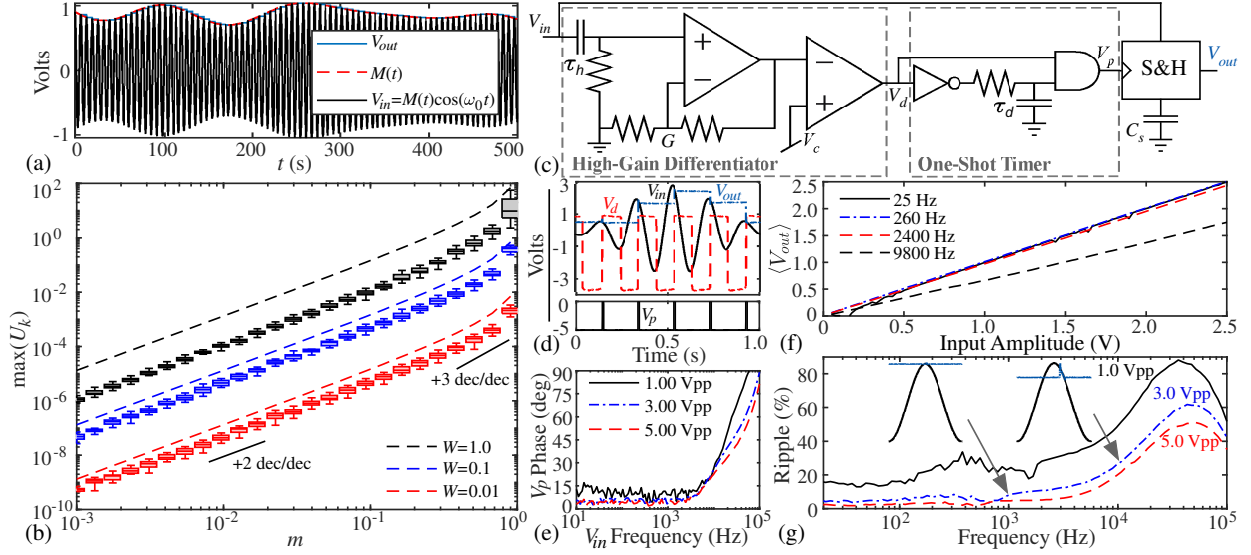
Fig. 4. MSED (a) exemplary response and (b) worst-case U under modulation generated from a pseudorandom bandlimited spectrum. In (b), the box-and-whiskers and dotted lines denote numerical trials and analytical bounds (Eq. 19), respectively. **Experimental** MSED (c) schematic and measured (d) waveforms as well as (e) S&H clock phase delay, (f) mean V_{out}, and (f) normalized ripple versus V_{in} frequency and amplitude. In (c), τ_h=1 μs, G=101, V_c=8 mV, τ_d=10 μs, and C_s=10 nF; the operational amplifiers (TL084) and S&H (LF398) run off ±5 V, and digital logic (74HC00) uses the negative rail.

Substituting Eq. 8 into Eq. 11 and assuming $|P_k| \ll 1/2\pi$:

$$U_k \approx 4\pi^2 P_k^2/3 + \pi P_k^3 + \left(1/4 - 8\pi^2/3\right) P_k^4 + \mathcal{O}\left(P_k^5\right). \quad (12)$$

Figure 2(f) compares partial sums of Eq. 12 to numerical simulations. When $|P_k| \ll 1/2\pi$, a second-order truncation closely matches simulation. For low P_k, U_k grows by 20 dB per decade of P_k; U_k growth rate tapers for large P_k.

C. Example: Estimated Bound for Sinusoidal Modulation

Sinusoidal modulation is relevant because output amplitude may oscillate in poorly tuned oscillator AGC loops. In such cases, amplitude modulation index is usually limited by higher-order nonlinearities [1]. Without loss of generality, let V_{in} be modulated at rate ω_m with index m, where $0 \le m < 1$:

$$V_{in}(t) = (1 + m \cdot \cos(\omega_0 w t)) \cos(\omega_0 t), \quad (13)$$

and $w := \omega_m/\omega_0$. Substituting Eq. 13 into Eq. 6 yields:

$$P_k = -w \cdot \sin(2\pi k w) / (\cos(2\pi k w) + 1/m). \quad (14)$$

By observing parity, we see that $\max P_k = -\min P_k$, so:

$$|P_k| \le w \cdot \max_{x \in [0,\pi]} \frac{\sin x}{\cos x + 1/m} = w \cdot m / \sqrt{1 - m^2}. \quad (15)$$

Hence: $\max(U_k) \approx \left(4\pi^2/3\right) w^2 m^2 / \left(1 - m^2\right). \quad (16)$

Figure 3 shows Eq. 16 and numerical simulation both coincide at low w and m, capturing the asymptotic 20 dB/dec rise of U_k relative to m; both show that $\max(U_k)$ spikes when $m > 0.5$.

IV. Bound by Marriage of Time and Frequency

While previous bounds are tight in their stated regimes, circuit designers usually know only a few time- and frequency-domain properties of V_{in} apriori: carrier rate (ω_0), amplitude modulation index (m), and modulation signal bandwidth (Ω).

We thus reformulate the bound on U_k using only these three properties. Without loss of generality, let: $M(t) = 1 + m \cdot \widetilde{M}(t)$, where $\widetilde{M}(t) \in [-1, 1]$ is bandlimited to Ω, and $0 \le m < 1$ to avoid phase reversal. The key step in our derivation is to bound $|P_k|$, which depends on $|\dot{M}(t)/M(t)|$. The tight Bernstein inequality [14] states that for any $f(t)$ bandlimited to Ω:

$$\left|\dot{f}(t)\right| \le \Omega \cdot \sup_{t \in \mathbb{R}} |f(t)|. \quad (17)$$

We can substitute $f(t) = \ln(M(t))$ into Eq. 17 to get:

$$|P_k| = \frac{1}{\omega_0} \left|\frac{\dot{M}}{M}\right| \le W \cdot \sup_{t \in \mathbb{R}} |\ln M| = -W \cdot \ln(1 - m), \quad (18)$$

where $W := \Omega/\omega_0$. Substituting Eq. 18 into Eq. 12 yields:

$$\max(U_k) \approx \left(4\pi^2/3\right) W^2 \ln^2(1 - m), \quad (19)$$

for $\max(U_k) < 1/3$. We validate Eq. 19 using Monte Carlo methods. Each trial synthesizes $\widetilde{M}[n]$ via iFFT of a single-sided, bandlimited spectrum with nonzero complex coefficients independently drawn from an uncorrelated bivariate normal distribution. Use of a 2^{20}-point iFFT and sampling rate of $1000\omega_0$ yields a long-duration, finely-resolved sequence, mitigating spectral artifacts in our approximation of $\widetilde{M}(t)$. Figure 4(a) shows a synthesized $M(t)$ and its corresponding demodulation. In Fig. 4(b), we characterize $\max(U_k)$ for a large set of such modulation signals across various m and W. Our numerical results confirm that Eq. 19 holds well when $\max(U_k) < 1/3$ and becomes tighter for large m and small W. Moreover, both Fig. 3 and Fig. 4(b) show that $\max(U_k)$ increases by 2 dec/dec relative to both the normalized bandwidth and the modulation index at low m and that V_{in} should have $m \ll 0.5$ for accurate MSED tracking.

V. DISCUSSION

The preceding discourse has highlighted the fundamental differences between NSEDs and MSEDs: in NSEDs, performance is limited by a latency–ripple trade off determined by circuit time constants, whereas in MSEDs, performance is determined by input signal properties—specifically, the modulation bandwidth relative to the carrier rate and the amplitude modulation index. Despite these differences, similarities and complementarities also coexist. Both architectures face large normalized errors if the modulation index approaches unity. NSEDs can also compensate the deficiencies of physical MSEDs at high carrier rates and vice-versa at low carrier rates.

Figure 4(c) shows a physical MSED implemented with commercially available ICs to highlight design trade-offs. As observed in the response to a sample input (Fig. 4(d)), MSEDs inherit the challenges of S&H circuits, such as charge injection, clock feedthrough, pedestal error, droopage, and nonlinear distortion—each active research topics [15], [16].

MSEDs face additional challenges as the carrier rate increases due to constraints in sample clock generation. Firstly, the high-gain differentiator needed to identify maxima exhibits limited bandwidth in practice [17]. As a result, the relative phase delay between the input signal and sample clock (V_p) increases markedly at high frequencies, as shown in Fig. 4(e); phase delay also increases at low input amplitudes and frequencies due to reduced differentiator output (V_d) slew rate.

Sample clock delay alters the effective sampling point, affecting output gain both at high input frequencies and at low input amplitudes and frequencies (Fig. 4(f)). The hold capacitor C_s (sized based on S&H nonidealities) sets the minimum sample pulse width for adequate settling, in-turn influencing output ripple. Figure 4(g) plots output ripple amplitude normalized to input amplitude. Ripple increases at high frequencies due to higher tracking phase duty cycles causing a greater portion of the input to feed through, until limited by S&H output buffer bandwidth. Normalized ripple also depends on input amplitude due to an additive, frequency-dependent contribution from charge injection and clock feedthrough.

To mitigate MSED limitations, [2] embeds the MSED between the rectifier and ripple filter stages of an NSED. This hybrid approach relaxes timing constraints on the MSED and suppresses ripple in both the high-frequency passthrough regime of the MSED and the low-frequency rectification-only regime of the NSED. The result is a flatter ripple profile, improved linearity, and a higher effective modulation cutoff frequency enabled by a relaxed NSED tuning.

VI. CONCLUSION

This work quantified how input properties affect MSED performance. We derived and validated bounds that show MSEDs perform best when modulation is slow relative to the carrier rate and when modulation index is low. We gave analytic results for exponential and sinusoidal modulation and offered practical "rules-of-thumb" for generic bandlimited signals. An experiment-driven discussion addressed physical considerations. These insights pave the way for broader adoption of MSEDs in wideband mixed-signal control systems and for further mathematical study of extrema-sampling systems.

REFERENCES

[1] B. Linares-Barranco, A. Rodriguez-Vazquez, E. Sanchez-Sinencio, and J. L. Huertas, "Generation, design and tuning of OTA-C high-frequency sinusoidal oscillators," *IEE Proceedings G - Circuits, Devices and Systems*, vol. 139, no. 5, pp. 557–568, 1992.

[2] S. Bhattacharyya and D. W. Graham, "Amplitude-regulated quadrature sine-VCO employing an OTA-C topology," *IEEE Transactions on Circuits and Systems II: Express Briefs*, vol. 70, no. 6, pp. 1886–1890, 2023.

[3] N. Pekcokguler, D. Morche, A. Burg, and C. Dehollain, "A high dynamic range envelop detector for heterodyne receiver architecture," *IEEE Transactions on Circuits and Systems II: Express Briefs*, vol. 71, no. 4, pp. 1929–1933, 2024.

[4] M.-G. Yu and D.-S. Kim, "Low-complexity ultrasonic flowmeter signal processor using peak detector-based envelope detection," *Journal of Sensor and Actuator Networks*, vol. 14, no. 1, 2025.

[5] B. Rumberg and D. W. Graham, "A low-power magnitude detector for analysis of transient-rich signals," *IEEE Journal of Solid-State Circuits*, vol. 47, pp. 676–685, 2012.

[6] Z.-H. C. Hui Liu, Li-Jun Zhang, "A novel RF envelope detector with ultra-wide operation frequency range and enhanced transient response speed," *IEICE Electronics Express*, 2017.

[7] J. Alegre, S. Celma, J. García del Pozo, and N. Medrano, "Fast-response low-ripple envelope follower," *Integration*, vol. 42, no. 2, pp. 169–174, 2009.

[8] M. Gazivoda and V. Bilas, "Always-on sparse event wake-up detectors: A review," *IEEE Sensors Journal*, vol. 22, no. 9, pp. 8313–8326, 2022.

[9] B. M. Kelly, A. T. DiLello, and D. W. Graham, "Reconfigurable analog preprocessing for efficient asynchronous analog-to-digital conversion," *Journal of Low Power Electronics and Applications*, vol. 9, no. 3, p. 25, 2019.

[10] S. Bhattacharyya and J. O. Hasler, "Extrema-triggered conversion for non-stationary signal acquisition in wireless sensor nodes," *Journal of Low Power Electronics and Applications*, vol. 14, no. 1, 2024.

[11] N. K. Sharma and T. V. Sreenivas, "Event-triggered sampling using signal extrema for instantaneous amplitude and instantaneous frequency estimation," *Signal processing*, vol. 116, pp. 43–54, 2015.

[12] F. M. et al., *Nonuniform Sampling Theory and Practice*, 1st ed., ser. Information Technology: Transmission, Processing and Storage. New York, NY: Springer US, 2001.

[13] R. Paley and N. Wiener, "Fourier transforms in the complex domain," *Mathematical Gazette*, vol. 19, no. 233, pp. 147–148, 1935.

[14] V. Totik, "Bernstein-type inequalities," *Journal of Approximation Theory*, vol. 164, no. 10, pp. 1390–1401, 2012.

[15] T. Iizuka, T. Ito, and A. A. Abidi, "Comprehensive analysis of distortion in the passive FET sample-and-hold circuit," *IEEE Transactions on Circuits and Systems I: Regular Papers*, vol. 65, no. 4, pp. 1157–1173, 2018.

[16] J. Jang, Y. Chae, and T. W. Kim, "A 1.5 V 2 GS/s 82.1 dB-SFDR track and hold circuit based on the time-divided post-distortion cancelation technique," *IEEE Transactions on Circuits and Systems II: Express Briefs*, vol. 69, no. 12, pp. 4719–4723, 2022.

[17] C. Mead, *Analog VLSI and neural systems*, ser. Addison-Wesley VLSI systems series. Reading, Mass: Addison-Wesley, 1989.